Application of the Weather Research and Forecasting Model for Air Quality Modeling in the San Francisco Bay Area

RAPHAEL E. ROGERS, AIJUN DENG, DAVID R. STAUFFER, AND BRIAN J. GAUDET

Department of Meteorology, The Pennsylvania State University, University Park, Pennsylvania

YIQIN JIA, SU-TZAI SOONG, AND SAFFET TANRIKULU

Bay Area Air Quality Management District, San Francisco, California

(Manuscript received 16 October 2012, in final form 10 May 2013)

ABSTRACT

The Weather Research and Forecasting (WRF) model is evaluated by conducting various sensitivity experiments over central California including the San Francisco Bay Area (SFBA), with the goal of establishing a WRF model configuration to be used by the Bay Area Air Quality Management District (BAAQMD) for its air quality applications. For the two selected cases, a winter particulate matter case and a summer ozone case, WRF solutions are evaluated both quantitatively by comparing the error statistics and qualitatively by analyzing the model-simulated mesoscale features. Model evaluation is also performed for the SFBA, Sacramento Valley, and San Joaquin Valley subregions. The recommended WRF configuration includes use of the Rapid Radiative Transfer Model/Dudhia (or RRTMG) radiation schemes and the Pleim–Xiu land surface physics, combined with a multiscale four-dimensional data assimilation strategy throughout the simulation period to assimilate the available observations, including standard observations from the World Meteorological Organization and local special observations. With the recommended model configuration, WRF is able to simulate the meteorological variables with reasonable error, with the added value, although relatively small, of assimilating the additional BAAQMD local special observations. Mesoscale features, simulated reasonably well for both cases, include the upslope and downslope flows that occur along the mountains that surround the Central Valley of California, as well as the mesoscale eddies that develop within the valley.

1. Introduction

Meteorological models commonly used to drive air-chemistry models for air quality study include the fifth-generation Pennsylvania State University–National Center for Atmospheric Research (Penn State–NCAR) Mesoscale Model (MM5; Grell et al. 1994), and the Weather Research and Forecasting model (WRF; Skamarock et al. 2008). These models can provide gridded meteorological fields that drive the air quality models to predict the concentrations of air pollutants, given the emissions information. Photochemical air quality models such as the Community Multiscale Air Quality (CMAQ) model (Byun and Schere 2006) and ENVIRON International Corporation's Comprehensive Air Quality Model with Extensions (CAMx; Kumar and Lurmann 1997) are widely used to simulate concentrations of particulate matter (PM), air toxins, and ozone. It has been shown that accurate meteorological conditions represented in numerical weather prediction models are critically important for air quality modeling (e.g., Tanrikulu et al. 2000; Deng et al. 2004; Otte 2008a,b).

The San Francisco Bay Area (SFBA) and the Central Valley (CV) region of California are two locations that constantly have high-pollution episodes due to their special topographical features (e.g., large flat valley interacting with both marine incoming flows and the mountain–valley circulations). Therefore, numerous modeling studies and air quality simulations have been made in an effort to reduce the amount of air pollution found in these two regions since the early 1990s (e.g., Stauffer and Seaman 1994; Seaman et al. 1995; Tanrikulu et al. 2000; Leidner et al. 2001). Seaman et al. (1995) demonstrated the value of using a multiscale four-dimensional data assimilation

Corresponding author address: Aijun Deng, Dept. of Meteorology, The Pennsylvania State University, 503 Walker Bldg., University Park, PA 16802.
E-mail: axd157@psu.edu

DOI: 10.1175/JAMC-D-12-0280.1

(FDDA) system in MM5 for simulations of episodes associated with high ozone concentrations in the San Joaquin Valley (SJV). The multiscale FDDA method from Stauffer and Seaman (1994) produces representative simulations of wind, temperature, moisture, and planetary boundary layer (PBL) heights, all of which are critical for air quality modeling.

The WRF model has been used in air quality studies in California. Bao et al. (2008) showed that WRF is capable of simulating reasonably well many of the low-level flows found in the CV. Michelson and Bao (2008) showed that for typical summertime synoptic conditions, winds simulated in the Sacramento Valley (SV) and the northern SJV are sensitive to large-scale forcing from the synoptic-scale flow. The winds simulated in the southern SJV are sensitive to soil initialization because the incoming marine flow veers into the SJV where it interacts and is modified by the upslope and downslope flows along the CV.

Soong et al. (2006) evaluated the performance of the MM5 and WRF models for an ozone episode in central California from 31 July to 2 August 2000, and found that both models simulated the wind and daytime temperatures quite well in the CV; however, in the SFBA region, both models overestimated the temperature along the coast by about 5°C and underestimated it in the SFBA inland valleys by 3°–5°C. For the nighttime, the WRF model overestimated temperatures by about 5°C in most areas. Similar to Bao et al. (2008) and Michelson and Bao (2008), the WRF experiment did not use FDDA since that capability was not available in WRF at the time of the study. Thus, one of our research goals is to improve WRF forecasts and evaluate the WRF performance over the SFBA region when FDDA is utilized.

The Bay Area Air Quality Management District (BAAQMD) has been using CMAQ and the CAMx models to simulate air pollutant concentrations in the SFBA region with meteorological inputs provided using MM5. Since the development of the MM5 system has been discontinued, the BAAQMD is interested in transitioning to WRF. The purpose of this study is to recommend a WRF model configuration for air quality modeling over the SFBA and CV regions during both the warm and cold seasons. Evaluations of the WRF model performance using different model physics and FDDA strategies are conducted, based on two high-pollution cases: one for winter and one for summer.

Section 2 gives a description of the WRF modeling system and the model physics and FDDA options used in this study. An overview of the two selected cases is presented in section 3. Section 4 details the configuration of the WRF model and the experimental design. Section 5 presents and describes the results of the model experiments using statistical (quantitative) analysis and subjective (qualitative) mesoscale analysis of the low-level wind patterns and flows. Section 6 presents a summary of the findings and conclusions.

2. Model description

The Advanced Research dynamics solver of the WRF model is the model of choice for this study and is fully documented in Skamarock et al. (2008). Similar to MM5, the WRF is a nonhydrostatic, fully compressible three-dimensional (3D) primitive equation model with a terrain-following, hydrostatic pressure vertical coordinate, and is designed for simulating atmospheric phenomena across scales ranging from large eddies (~100 m) to mesoscale circulations and waves (from ~100 m to 1000 km) to synoptic-scale weather systems (≥1000 km).

The WRF modeling system encompasses a variety of physics options for microphysics, cumulus parameterization, atmospheric radiation, and planetary boundary layer (PBL) turbulence physics and land surface models (LSMs). For microphysics, this study uses the WRF single-moment three-class (WSM3) simple ice scheme (Hong et al. 2004) that assumes no mixed-phase conditions. For cumulus parameterization, the Kain–Fritsch scheme (Kain and Fritsch 1990; Kain 2004) is used on the coarser grids. Two suites of radiation schemes are compared: the Rapid Radiative Transfer Model (RRTM; Mlawer et al. 1997) longwave (LW)/Dudhia shortwave (SW; Dudhia 1989) scheme and the RRTM for general circulation models (GCMs) scheme (RRTMG; Iacono et al. 2008). As in MM5, the RRTM scheme is used for LW radiation in combination with the Dudhia SW scheme (Dudhia 1989). The RRTMG scheme can be used for both LW and SW. It is similar to RRTM but with improved efficiency for GCM applications, and a recent intercomparison study showed that RRTMG had extremely small mean errors in solar flux at the surface and at the top of the atmosphere (Oreopoulos et al. 2012).

Two different PBL physics schemes are used in this study: the turbulent kinetic energy (TKE)-predicting Mellor–Yamada level-2.5 turbulent closure scheme (MYJ PBL; Janjić 1996, 2002) and the Asymmetrical Convective Model, version 2 (ACM2), which is designed for the Pleim–Xiu (PX) physics suite (Pleim 2007). The difference between the two is that the MYJ is a local scheme in which the vertical mixing within the same time step is allowed only between the adjacent model layers and the PBL depth is determined by the TKE profile, while ACM2 is a scheme with both local diffusion and nonlocal transport terms, and the PBL depth is determined by the stability.

For land surface processes, the five-layer thermal diffusion scheme is evaluated along with three other LSMs:

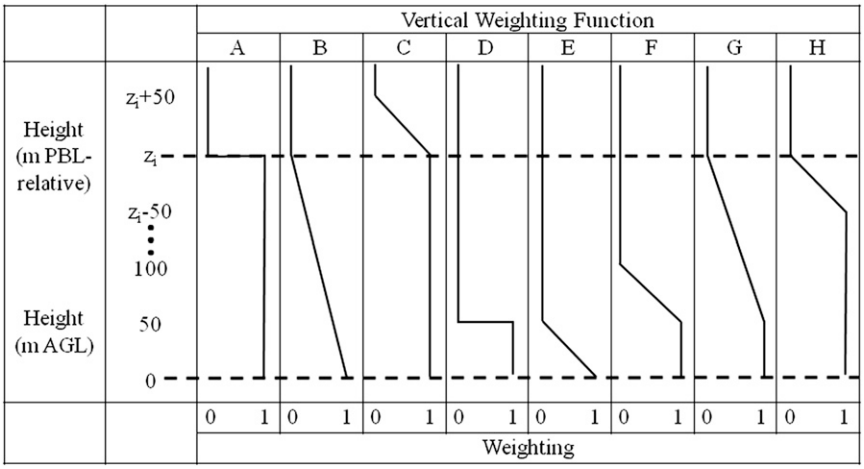

FIG. 1. Illustration of possible vertical weighting functions for surface observations. For each of the eight examples, the horizontal axis is the weight (from 0 to 1) and the vertical axis is the height from 0 (the ground) to z_i + 50 (50 m above the top of the PBL). The dashed horizontal lines indicate the surface and the PBL top. Column C is the default function for the unstable PBL regime, and column F is the default function for the stable PBL regime.

1) Noah LSM (Chen and Dudhia 2001), 2) Rapid Update Cycle LSM (RUC, Smirnova et al. 1997, 2000), and 3) PX LSM (Xiu and Pleim 2001; Pleim and Xiu 2003; Gilliam and Pleim 2010). The five-layer thermal diffusion scheme is a soil temperature–only scheme, with constant soil moisture values. The Noah LSM is a four-layer soil temperature and moisture scheme and includes root zone, evapotranspiration, soil drainage, and runoff, taking into account vegetation categories, monthly vegetation fraction, and soil texture. The scheme can predict soil ice and snow cover. The RUC LSM is a six-level soil temperature and moisture scheme that contains a snow model that can account for changing snow density, snow depth, refreezing liquid water, and fractional snow cover. The PX LSM is a two-layer soil temperature and moisture model, similar to Noah and RUC, except that it contains two indirect nudging schemes involved in the PX LSM. In the first scheme, soil moisture is nudged according to the biases in 2-m air temperature and relative humidity (RH) between the model- and observation-based analyses (Pleim and Xiu 2003). In the second scheme, the deep soil temperature in the soil temperature force–restore model is also nudged according to the model bias in 2-m air temperature, but only during nighttime (Pleim and Gilliam 2009).

The WRF modeling system also has FDDA capabilities similar to those in MM5. The version of FDDA used in this research was originally developed for MM5 at Penn State (Stauffer and Seaman 1990, 1994) and was recently enhanced and implemented into WRF (Deng et al. 2009). Further enhancements to the observation, or obs, nudging technique in WRF have brought more flexibility to control how surface observations influence meteorology in aloft layers. As illustrated in Fig. 1, WRF users have freedom to choose different vertical weighting functions for the surface observations. In contrast, the MM5 obs nudging capability is fixed to have surface winds influence the lowest three model layers with

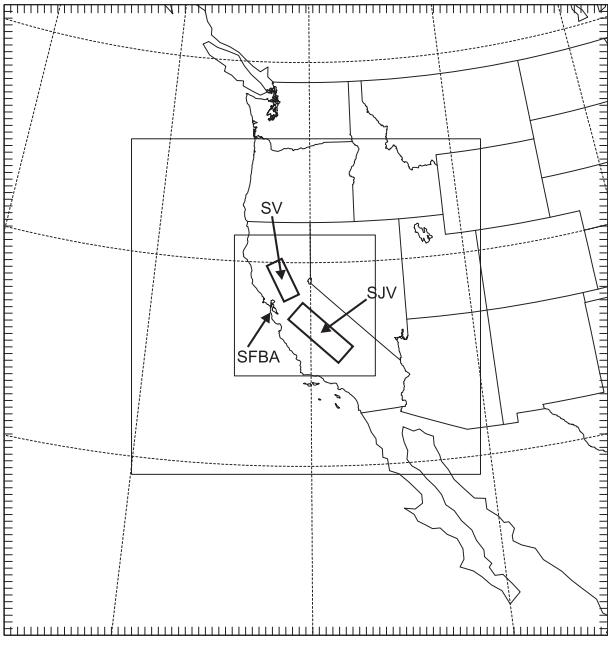

FIG. 2. WRF nested grids showing the 4- (innermost), 12- (middle), and 36-km (outermost) grids. Locations of San Francisco Bay Area, Sacramento Valley and San Joaquin Valley are indicated by SFBA, SV and SJV, respectively.

TABLE 1. FDDA configuration for WRF simulations for the winter PM case.

	36 km		12 km		4 km	
Expt	Analysis nudging	Obs nudging	Analysis nudging	Obs nudging	Analysis nudging	Obs nudging
NOFDDA	No	No	No	No	No	No
GFDDA	Yes	No	Yes	No	No	No
OFDDA	No	Yes	No	Yes	No	Yes
MFDDA	Yes	Yes	Yes	Yes	No	Yes
MFDDAwSP	Yes	Yes	Yes	Yes	No	Yes

linearly decreasing weights. WRF allows the surface observations to be spread through the entire PBL with full strength for the unstable PBL regime (column C), and then the weights decrease linearly to zero 50 m above the PBL top. For the stable PBL regimes, as the default, WRF allows the surface observations to be spread upward to 50 m with full strength and then to linearly decrease to zero for the next 50 m (column F). The default surface data weighting functions (columns C and F) are used for this study.

3. Case description

Two air pollution cases are chosen for this study: a winter PM case starting at 1200 UTC 16 December and ending at 1200 UTC 21 December 2000, representing the cold-season weather conditions, and a summer ozone case starting at 1200 UTC 29 July and ending at 1200 UTC 3 August 2000, representing the warm-season weather conditions. As is typical for many air-pollution cases, there was very little cloud and precipitation throughout the study period for both periods of study.

The winter case period began at 1200 UTC 16 December 2000 with an inverted trough just off the coast of California, associated with a surface high over northern Nevada and a high to the west of the trough over the Pacific Ocean. Temperatures were cooler over the land than over the ocean, leading to easterly winds flowing offshore. The winds over the SFBA and within the CV were very light and northerly or northwesterly. Upper-air analyses show that high pressure was centered over western Nevada at the 850-hPa level (not shown) and a ridge was over the entire western coastline of the United States at 500 hPa. The upper-level high and 500-hPa ridge helped to reinforce the stable conditions at the surface. These stable conditions allowed for the development of an elevated PM episode.

Over the next 3 days the surface high off the California coast strengthened and moved onshore over Utah and California and maintained stable conditions. The surface high and the ridge at both the 850- and 500-hPa levels persisted throughout this time. On 21 December, troughs moved in from the Pacific Ocean at both the surface and the 850-hPa level, signifying the end of the PM episode; however, the ridge remained at 500 hPa, maintaining weak synoptic conditions.

At the beginning of the PM episode, 24-h concentrations of particulate matter smaller than 2.5 μm in diameter (PM2.5) were moderate in the SFBA, as well as in the Sacramento area, about 14 and 20 $\mu g\,m^{-3}$, respectively. In the SJV, it was above the 24-h standard, around 39 $\mu g\,m^{-3}$. As the episode developed, concentrations increased throughout the study region, reaching 35 $\mu g\,m^{-3}$ at San Jose, 37 $\mu g\,m^{-3}$ at Sacramento, 48 $\mu g\,m^{-3}$ at Fresno, and 53 $\mu g\,m^{-3}$ at Bakersfield. Starting from 20 December, concentrations significantly dropped in the SFBA and the Sacramento area, to around 20 $\mu g\,m^{-3}$. The decrease was moderate in the

TABLE 2. Multiscale FDDA parameters used in this study, where G is the nudging coefficient, RINXY is the horizontal RIN used in obs nudging, and TWINDO is the time window used in obs nudging. Note that RINXY is reduced by a factor of 0.5 for the surface and increased by a factor of 2 at 500 hPa and above; TWINDO is reduced by a factor of 0.5 for the surface. Here, N/A indicates not applicable.

	Analysis nudging			Obs nudging		
	36 km	12 km	4 km	36 km	12 km	4 km
G ($1\,s^{-1}$)	0.0003	0.0001	N/A	0.0004	0.0004	0.0004
3D wind field	Nudging all layers	Nudging all layers	N/A	Nudging all layers	Nudging all layers	Nudging all layers
3D mass field	Nudging above PBL	Nudging above PBL	N/A	Nudging above PBL	Nudging above PBL	Nudging above PBL
Surface wind field	Used within PBL	Used within PBL	N/A	Used within PBL	Used within PBL	Used within PBL
Surface mass field	Not used	Not used	N/A	Not used	Not used	Not used
RINXY (km)	N/A	N/A	N/A	150	100	100
TWINDO (h)	N/A	N/A	N/A	2	2	2

TABLE 3. FDDA configuration for WRF simulations for the summer ozone case.

	36 km		12 km		4 km	
Expt	Analysis nudging	Obs nudging	Analysis nudging	Obs nudging	Analysis nudging	Obs nudging
NOFDDA	No	No	No	No	No	No
MFDDA	Yes	No	Yes	Yes	No	Yes
MFDDAwSP	Yes	No	Yes	Yes	No	Yes

SJV, to around 40 $\mu g\,m^{-3}$. Note that the majority of the stations collected PM2.5 data every third day but not necessarily on the same days.

The summer ozone case for this study is the same case used by Bao et al. (2008). This period began at 1200 UTC 29 July 2000 with a surface heat low south of the SJV and an inverted trough extending from the low over several West Coast states. High temperatures over the land led to onshore flow along the coast with westerly winds extending over the SFBA and into the CV. High pressure areas at both 850- and 500-hPa levels helped to reinforce the stable conditions and light winds at all three levels (i.e., surface, and 850 and 500 hPa). These conditions led to the onset of the ozone episode during this period. The synoptic conditions persisted throughout the period with the surface heat low located over California, and large high pressure systems at the 850- and 500-hPa levels over the West Coast to maintain the weakly forced conditions, thus allowing for high concentrations of ozone to persist over the SFBA and the CV for days.

Ozone exceedance areas changed from region to region during the summer ozone episode. Ozone exceeded the federal 1-h standard (124 parts per billion, or ppb) in the SFBA on 31 July, in the Sacramento area on 1 August, and in the SJV on 2 August. The ozone exceedance in the SFBA occurred at Livermore (126 ppb) at 1600 Pacific standard time (PST), in the Sacramento area at Sloughhouse (133 ppb) at 1400 PST, and in SJV at Edison (151 ppb) at 1300 PST.

4. Experimental design

a. WRF modeling configuration

This research uses WRF, version 3.2.1, with the grid configuration composed of three nested grids with 36-, 12-, and 4-km grid spacings, with grid dimensions of 91 × 95 for the 36-km grid and 157 × 151 for the 12-km grid (Fig. 2). The 4-km grid, with a horizontal mesh of 190 × 190 grid points, contains the entire central California air quality modeling grid. It consists of the SFBA and the CV region that contains both the SV and the SJV. Fifty vertical layers are used in all numerical experiments for all grids. The lowest half layer is located at ~12 m above ground level (AGL). The thickness of the layers increases gradually with height, with 27 layers below 850 hPa (~1550 m AGL). The top of the model is defined at 100 hPa. One-way nesting is used for all experiments so that information from the coarse grids translates to the lateral boundaries of the fine grids but no information from the fine grids translate to the coarse grids. Our primary interest is in the 4-km grid that is identical to the air quality modeling grid routinely used at BAAQMD.

b. Data sources and description

To provide an effective FDDA on the 4-km grid, meteorological observations with mesobeta-scale (20–200 km) resolution are needed. The conventional World Meteorological Organization (WMO) observations (i.e., wind speed, wind direction, temperature, and dewpoint temperature) from the National Weather Service have sufficient resolution for synoptic-scale and mesoalpha-scale (200–2000 km) phenomena but not for

TABLE 4. WRF-simulated surface-layer MAEs for the winter PM case, averaged over the entire 5-day period and over the entire grid for each grid, starting 1200 UTC 16 Dec and ending 1200 UTC 21 Dec 2000, comparing four LSMs. The units for this and subsequent tables are percent for RH, degrees Celsius for temperature, degrees for wind direction, and meters per second for wind speed.

	36 km	12 km	4 km
RH			
Thermal diffusion	16.7	18.4	16.9
Noah	14.4	16.3	19.1
RUC	14.9	15.8	16.6
Pleim–Xiu	13.9	15.3	17.8
Temperature			
Thermal diffusion	2.8	2.6	2.5
Noah	2.9	2.7	2.5
RUC	2.8	2.6	2.5
Pleim–Xiu	2.7	2.4	2.0
Wind direction			
Thermal diffusion	49	53	48
Noah	49	53	47
RUC	49	52	49
Pleim–Xiu	49	52	47
Wind speed			
Thermal diffusion	2.5	1.9	1.6
Noah	2.6	2.0	1.6
RUC	2.4	1.8	1.6
Pleim–Xiu	2.2	1.7	1.5

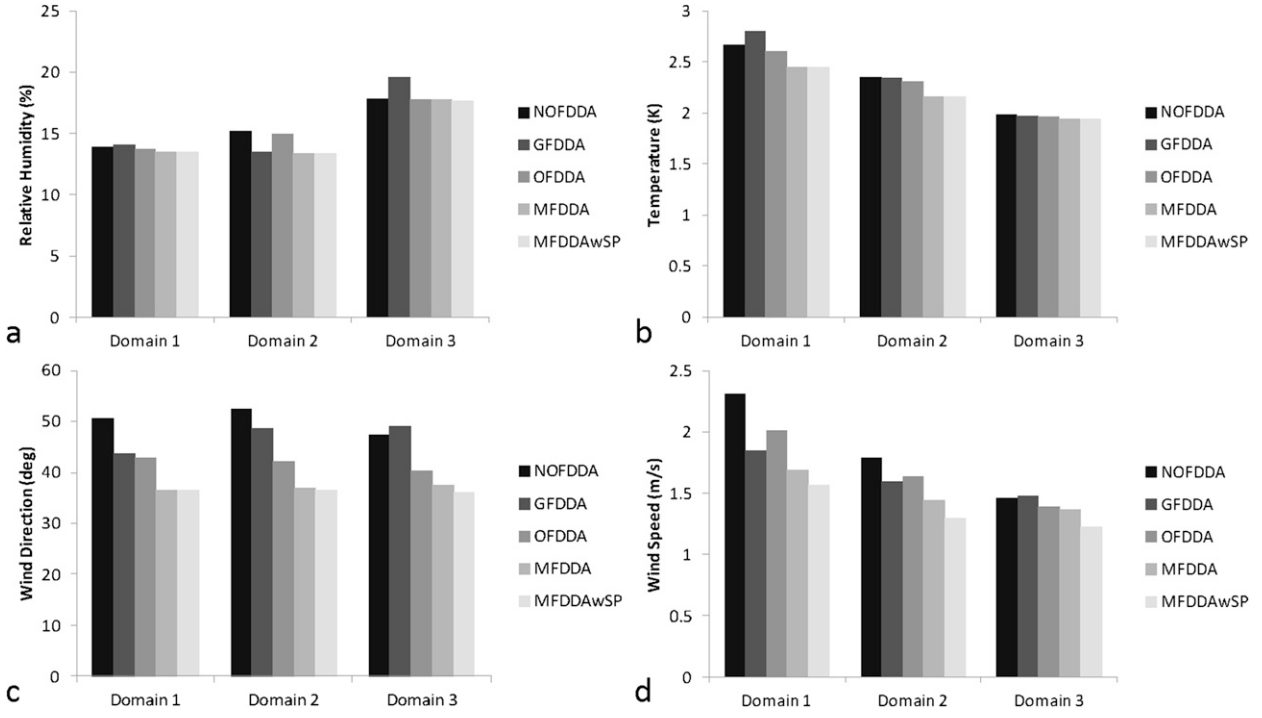

FIG. 3. Surface MAEs for the winter PM case, averaged over the entire 5-day period and over the entire grid for each grid, starting 1200 UTC 16 Dec and ending 1200 UTC 21 Dec 2000 for the five FDDA numerical experiments for the WRF-simulated fields: (a) RH, (b) temperature, (c) wind direction, and (d) wind speed.

the mesobeta-scale phenomena that can occur within the CV and over the SFBA. Therefore, additional data from two separate sources were obtained for this study: routine surface data collected by the local air quality management districts (referred to as AQS stations), and upper-air data collected during the California Regional Particulate Air Quality Study (Watson et al. 1998). For the surface, in addition to the WMO observations, 97 AQS stations for the winter PM case and 94 for the summer ozone case are used for FDDA. Additional surface stations (67 for the winter PM case and 72 for the summer ozone case) are not used in FDDA, but are used for independent verification. For the upper air, in addition to the WMO observations, the upper-air wind observations from the 19 wind profiler stations are assimilated.

All WRF simulations use the National Centers for Environmental Prediction (NCEP)–NCAR 40-km Eta Model analyses for the initial conditions and lateral boundary conditions (ICs/LBCs). The IC fields are further enhanced by rawinsonde and surface data through the WRF objective analysis process, Obsgrid (Deng et al. 2009), using a modified Cressman analysis (Benjamin and Seaman 1985). The 3D analyses used for analysis-nudging FDDA are also enhanced by the objective analysis process and are defined at 6-h intervals, while the surface analysis fields used for surface analysis FDDA are generated by Obsgrid at 3-h intervals. All the observations are quality checked for erroneous data. These quality-checked observations are used for both obs nudging and model verification.

c. *Model experiments*

To achieve our goal of determining a recommended model configuration, various WRF experiments, with varying model physics and FDDA options, are conducted. The investigation starts with comparing the use of two radiation schemes, followed by comparing the use of various LSMs to determine a recommended LSM for the region. Since the cases chosen in this study are relatively dry, it is important to note that varying microphysics schemes, cumulus parameterizations, and radiation schemes will most likely not have an impact on the simulations. Using the preferred model physics found as the result of the sensitivity study for atmospheric radiation, PBL, and the land surface processes as the baseline model configuration, a set of WRF experiments with varying FDDA strategies is conducted.

For the winter PM case, five FDDA simulations are performed (Table 1): 1) NOFDDA, where no data assimilation of any form is applied; 2) GFDDA, where 3D (excluding surface) analysis nudging is used on the 36- and 12-km grids; 3) OFDDA, where only obs nudging

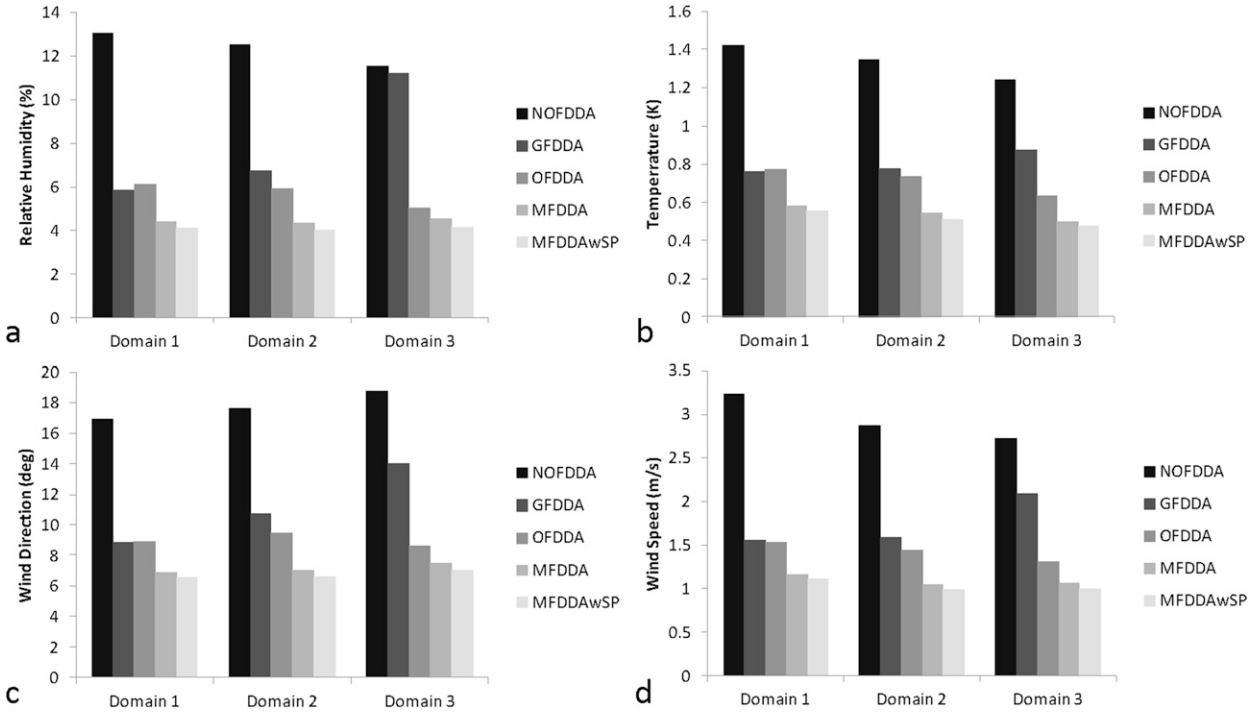

FIG. 4. As in Fig. 3, but for upper-air MAEs.

is used on all three grids, assimilating WMO and special wind profiler data; 4) MFDDA, an experiment combining 3D analysis nudging (on the 36- and 12-km grids), surface analysis nudging, and obs nudging (on all grids) within a multiscale FDDA framework, assimilating only WMO observations; and 5) MFDDAwSP, which is identical to MFDDA except that in addition to the WMO observations, the 19 wind profiler and 97 surface observations from the AQS meteorological network are also assimilated. Note that for each FDDA experiment, FDDA is used for the entire 5 days.

The FDDA strategies and the parameters used in the FDDA experiments are shown in Table 2. Nudging of the wind field is applied through all model layers, but nudging of the mass fields (temperature and moisture) is only allowed above the model-simulated PBL so that the PBL structure produced by the model is dominated by the model physics. The radius of influence (RIN) for the surface data is reduced to 50 km, as suggested by Seaman et al. (1995) (i.e., by multiplying a factor of 0.5 to the specified value in Table 2) in obs nudging. Note that as indicated in Table 2, within the multiscale FDDA framework, similar to the 36-km grid, the analysis nudging is also applied on the 12-km grid with reduced strength (from 0.0003 to 0.0001 s^{-1}). This is designed to allow the FDDA to be effective in reducing the model errors on the 4-km grid but at the same time not causing the mesobeta-scale features to be smoothed out by the FDDA.

For the summer ozone case, based on the lessons learned from the winter case, no individual FDDA experiments (e.g., analysis nudging only or obs nudging only) are conducted. Only three model simulations are conducted, as indicated in Table 3: 1) NOFDDA; 2) MFDDA, similar to the MFDDA experiment from the winter PM case, only the WMO surface and upper-air observations are assimilated; and 3) MFDDAwSP, similar to the MFDDAsWP from the winter case, with the 94 AQS surface observations also assimilated. Note that MFDDAwSP is set up slightly differently (i.e., no wind profiler data are available). The FDDA parameters for the summer case are the same for the winter case shown in Table 2.

5. Meteorological model results

Evaluation of the WRF-simulated meteorological features is accomplished by both quantitative and qualitative approaches. Quantitative evaluation is performed by comparing the error statistical scores of the model-simulated wind speed, wind direction, temperature T, and RH. Mean absolute error (MAE) is calculated to measure how close the model values are compared to the observed values. Mean error (ME) is calculated to

TABLE 5. WRF-simulated surface-layer MAEs verified against the AQS independent observation dataset, for the winter PM case, averaged over the entire 5-day period and over the entire grid for each grid, starting 1200 UTC 16 Dec and ending 1200 UTC 21 Dec 2000, comparing NOFDDA and MFDDAwSP. Note that RH was unavailable.

	36 km	12 km	4 km
Temperature			
NOFDDA	2.8	2.4	2.2
MFDDAwSP	2.6	2.3	2.2
Wind direction			
NOFDDA	67	55	50
MFDDAwSP	56	48	44
Wind speed			
NOFDDA	1.7	1.5	1.3
MFDDAwSP	1.3	1.3	1.2

measure the model bias for a given variable. MAE and ME are computed for both the surface and upper air. For the surface, the model values from the lowest model layer are compared with the surface observations. For the upper air, the model values are interpolated onto the observation locations in both horizontal and vertical pressure space, and are then compared with the observations. A calm wind threshold was used in this study to remove the very light winds (less than or equal to 1 m s^{-1}) for the wind direction statistics calculation because the wind direction for near-calm wind is uncertain.

Horizontal charts of the WRF-simulated fields are made at different vertical levels in order to qualitatively analyze how well the model simulates these meteorological variables. The simulations are also analyzed to determine if the model can capture and reasonably simulate the mesoscale features that are specific to the study region, such as the upslope and downslope flows along the valley walls, the air flows into and out of the CV, and the mesoscale eddies. Time series plots of simulated and observed winds and temperature are also produced to help indicate how well the modeled and observed values compare at individual locations.

a. Winter PM case

1) QUANTITATIVE VERIFICATION

The investigation began by comparing between the WRF solutions found using the RRTM/Dudhia and the RRTMG suites of radiation schemes. The MAE shows that both radiation suites produce similar results for all four meteorological variables (not shown). Since there is no clear winner in the MAEs, either the RRTM/Dudhia or the RRTMG radiation suite can be selected. However, since the RRTM/Dudhia radiation suite has been in MM5 and WRF for years and has been well tested (a critical factor for an operational model configuration), it is chosen for all the numerical experiments conducted in this study.

The next step is to evaluate the model performance with different LSMs. The MAEs of the WRF-simulated fields are compared among the five-layer thermal diffusion scheme, the Noah LSM, the RUC LSM, and the

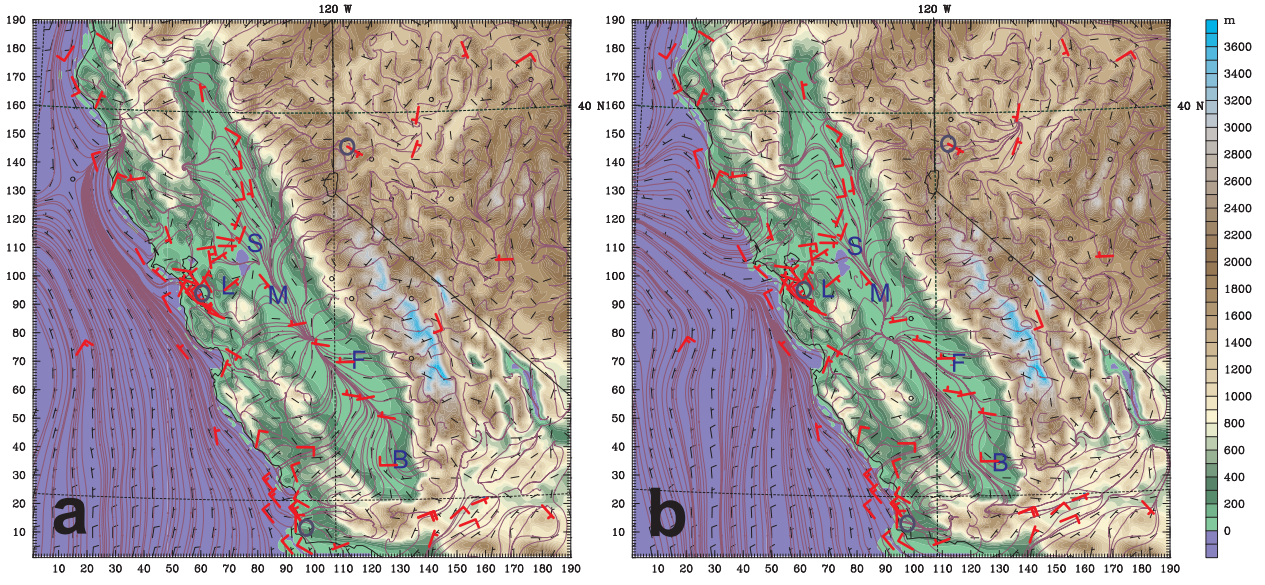

FIG. 5. WRF-simulated surface layer winds on the 4-km grid, overlaid with WMO observations at 0000 UTC 17 Dec 2000 for (a) NOFDDA and (b) MFDDAwSP for the winter PM case. Note that the large open circles denote the locations of the three WMO upper-air stations (Oakland, CA; Reno, NV; and Vandenberg Air Force Base, CA), and other symbols mark the locations of Livermore (L), Fresno (F), Sacramento (S), Bakersfield (B), and Modesto (M). The background shading shows the terrain elevation (m).

PX LSM. Note that the soil temperature and moisture fields needed to initialize the LSMs are derived from the NCEP–NCAR 40-km Eta Model analyses. Table 4 shows the MAEs of the WRF-simulated surface-layer fields for the winter PM case. Comparing the PX results with the results of the Noah and RUC models, as well as the five-layer thermal diffusion scheme, it is found that overall using the PX physics has a quite positive impact (except for the 4-km grid RH field that is slightly worse than that in the thermal diffusion and RUC LSM experiments). Wind directions are comparable among all four experiments, with PX having a slight advantage on the 4-km grid. Based on this evaluation, the PX LSM will be used as part of the baseline configuration for the FDDA simulations, along with the RRTM radiation scheme.

It is worth pointing out that our sensitivity experiments (not shown) indicated that with the use of soil temperature and moisture nudging, WRF solutions generally show some improvement in the surface moisture and temperature fields for the 36- and 12-km grids where the surface analysis nudging is used, and the improvements are more evident for temperature. It should also be noted that, ideally, better results could be achieved if the model is run for at least 10 days to allow the deep soil temperature to spin up, as suggested by Gilliam and Pleim (2010).

To demonstrate the effectiveness of FDDA in reducing model errors, Fig. 3 shows the MAEs of the WRF-simulated surface fields for the five experiments that use the combination of FDDA methods described previously, averaged over the entire 5-day period and over the entire grid for each grid. The MAEs are computed using the observations assimilated in obs nudging; thus, they measure the "closeness to fit" statistics. Note that comparing MFDDA with MFDDAwSP demonstrates the effect of assimilating the observations from the AQS meteorological network. Also note that it is not our intention to compare the statistical scores between different model grids due to the different numbers of observations used in the verification. It is shown in the surface MAE comparison for RH and T (Figs. 3a and 3b) that although the nudging of the mass fields is excluded from the PBL, the indirect improvement due to the use of FDDA is still evident for each grid, especially in both MFDDA experiments on the 36- and 12-km grids. The MEs of the WRF-simulated surface RH and T for both MFDDA experiments (not shown) show very small dry biases (<5% on the 36- and 12-km grids and ~10% on the 4-km grid) and little temperature bias on all grids. Note that both of these statistics are comparable to the previous model studies, indicating a very good simulation. For example, the simulated MAEs of $\sim 1.6\,\mathrm{m\,s^{-1}}$ on the 36-km grid and $\sim 1.4\,\mathrm{m\,s^{-1}}$ on the 12-km grid are similar to those reported in Gilliam et al. (2006) on the same resolution grids; the MAE value of $\sim 1.3\,\mathrm{m\,s^{-1}}$ on the 4-km grid is better than that reported in Schroeder et al. (2006).

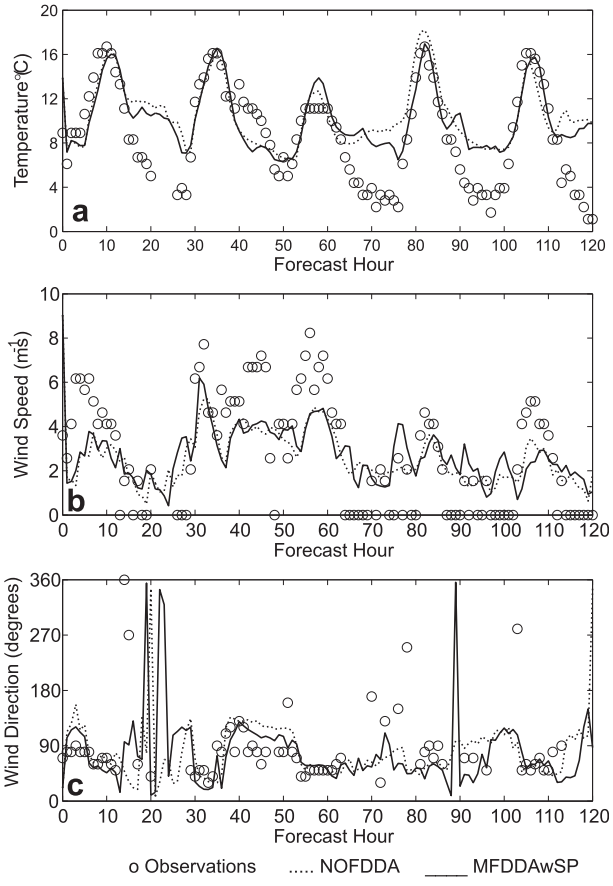

FIG. 6. WRF-simulated fields and the observed surface time series plot for Livermore for the winter PM case starting 1200 UTC 16 Dec and ending 1200 UTC 21 Dec 2000 for (a) temperature, (b) wind speed, and (c) wind direction.

For wind fields, the use of FDDA clearly reduces the MAE errors (Figs. 3c and 3d). Using multiscale FDDA greatly reduces the wind direction MAE errors (by more than 10° or about 25% in MFDDAwSP) relative to the NOFDDA experiment. The errors are more significantly reduced because the winds are assimilated at the surface, unlike the moisture and the temperature. Because this is a weakly forced case with light winds, the wind speed MAEs are generally small, as expected, even without FDDA. Notice that on the 4-km grid, GFDDA does not show improvement since analysis nudging is not used. It is clear that the multiscale experiment, MFDDAwSP, produced the smallest errors. The MEs (not shown) indicated that the model wind speed tends to be slightly greater than the observations. For example on the 4-km grid, WRF wind speeds are $0.5\,\mathrm{m\,s^{-1}}$ too large in all experiments except MFDDAwSP (i.e., only $\sim 0.1\,\mathrm{m\,s^{-1}}$), which indicates the FDDA is slowing down the wind speeds.

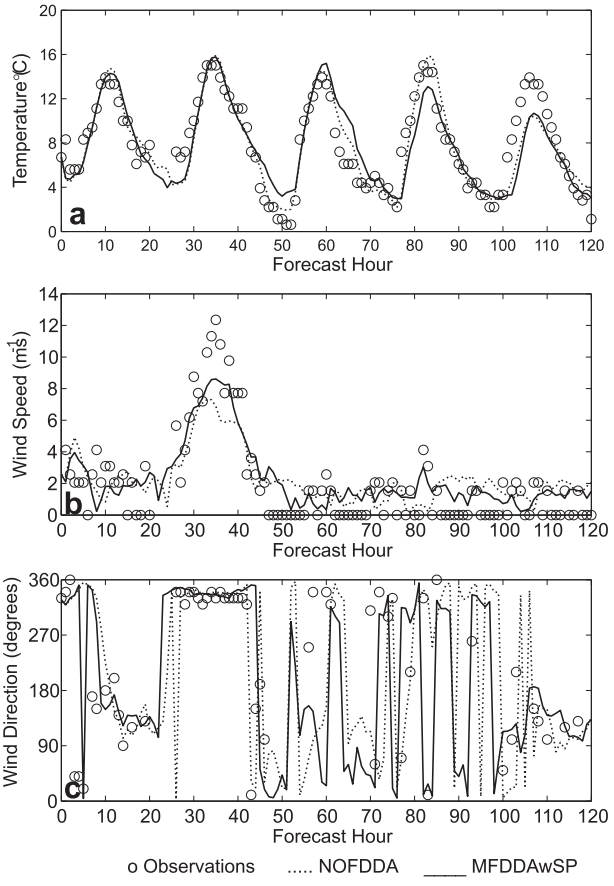

FIG. 7. As in Fig. 6, but for Sacramento.

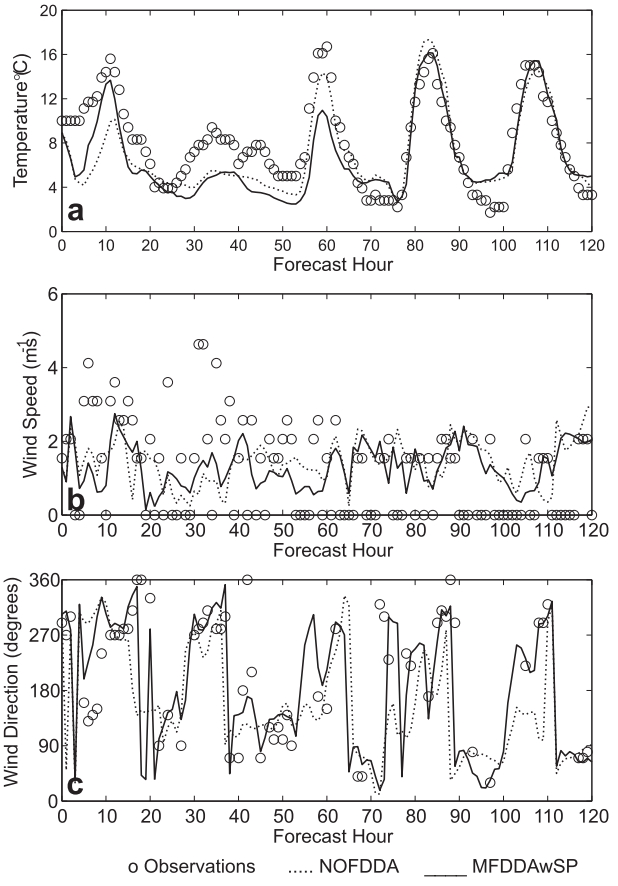

FIG. 8. As in Fig. 6, but for Fresno.

The effectiveness of using FDDA is evident for the upper air (Fig. 4). It is shown that for all four meteorological fields, both analysis-nudging and obs-nudging experiments alone significantly improve the model performance, with obs nudging being more effective than analysis nudging on finer grids. Both MFDDA experiments that combine the analysis nudging on the 36- and 12-km grids with the obs nudging on all three grids produce the best results. The upper-air MEs (not shown) indicate that model solutions overall, especially when improved with FDDA, have little bias for any of the four fields (e.g., $<1\%$ for RH, <0.25°C for T, <2° for wind direction, and $<0.1\,\mathrm{m\,s^{-1}}$ for wind speed, for all grids).

Comparing MFDDA and MFDDAwSP shows an added value of assimilating the special AQS observations and the wind profilers from the BAAQMD meteorological network. For the surface such an effect is more evident for wind fields (Figs. 3c and 3d). For upper air, the added value is evident for all fields (Fig. 4). It should be noted that the added value is relatively small since model errors have already been significantly reduced by assimilating WMO observations.

Note that the model verifications discussed above were based on the entire set of the WMO and special observations that have been assimilated. To demonstrate the effectiveness of FDDA, it is important to show how the model performs against the independent observations that were not assimilated. Table 5 shows the surface MAE comparing NOFDDA and MFDDAwSP verified against the independent AQS observation dataset (i.e., 67 stations) for the winter PM case. Note that RH was not available for this data source. It is shown that there is a clear benefit in using FDDA for all fields and for all grids (except for the 4-km-grid T).

Although the grid-wide statistics show that FDDA improves the model skill, the model performance could vary from region to region. It is the interest of BAAQMD to spatially verify model solutions for specific subregions. For this research, MAE scores are also computed for the three subregions individually: 1) the SFBA, 2) the SV, and 3) the SJV. It was found that the FDDA did not improve the surface wind directions for the SFBA as much as for the entire grid (i.e., 14° improvement for the entire 4-km grid versus 7° improvement for the

TABLE 6. WRF-simulated surface-layer MAEs, for the summer ozone case, averaged over the entire 5-day period and over the entire grid for each grid, starting 1200 UTC 29 Jul and ending 1200 UTC 3 Aug 2000, comparing three LSMs.

	36 km	12 km	4 km
RH			
Noah	12.1	12.5	11.8
RUC	13.0	12.8	14.1
Pleim–Xiu	12.2	13.2	12.4
Temperature			
Noah	2.7	3.0	2.9
RUC	2.5	2.7	2.7
Pleim–Xiu	2.7	3.2	3.0
Wind direction			
Noah	56	54	49
RUC	56	55	49
Pleim–Xiu	57	55	48
Wind speed			
Noah	1.6	1.6	1.5
RUC	1.7	1.6	1.6
Pleim–Xiu	1.6	1.6	1.7

SFBA), most likely due to limited representativeness in the observed surface wind directions due to the complexity of the coastal characteristics, or insufficient model resolutions. The same can be said for the RH and the T in both the SV (i.e., 5% degradation in RH and 0.2°C degradation in T) and the SJV (i.e., no improvement in RH and 0.1°C degradation in T).

2) QUALITATIVE VERIFICATION

On the 36-km grid both NOFDDA and MFDDAwSP are quite comparable with each other at the surface and in the upper air. Both simulations do well in representing the locations of surface highs and lows, as well as the temperatures and the flow along the coast and CV (not shown). The ridges and highs at 850 and 500 hPa are also well represented. FDDA allows the MFDDAwSP to simulate the temperature gradient and the direction of the flow in better agreement with the observations than does the NOFDDA experiment.

On the 4-km grid the effects of FDDA are quite evident. Figure 5 shows sample plots of the simulated wind field overlaid with the WMO observations on the entire 4-km grid. The plots are for 0000 UTC 17 December 2000, which is 12 h into the simulation and during the daytime (1600 PST on 16 December 2000). The simulated winds for NOFDDA show that even without FDDA the model does a reasonable job of resolving the mesoscale features that comprise this specific region. However, NOFDDA (Fig. 5a) shows large wind direction errors over the CV. At some locations the directions of the winds vary by as much as 90°, such as near Bakersfield in the

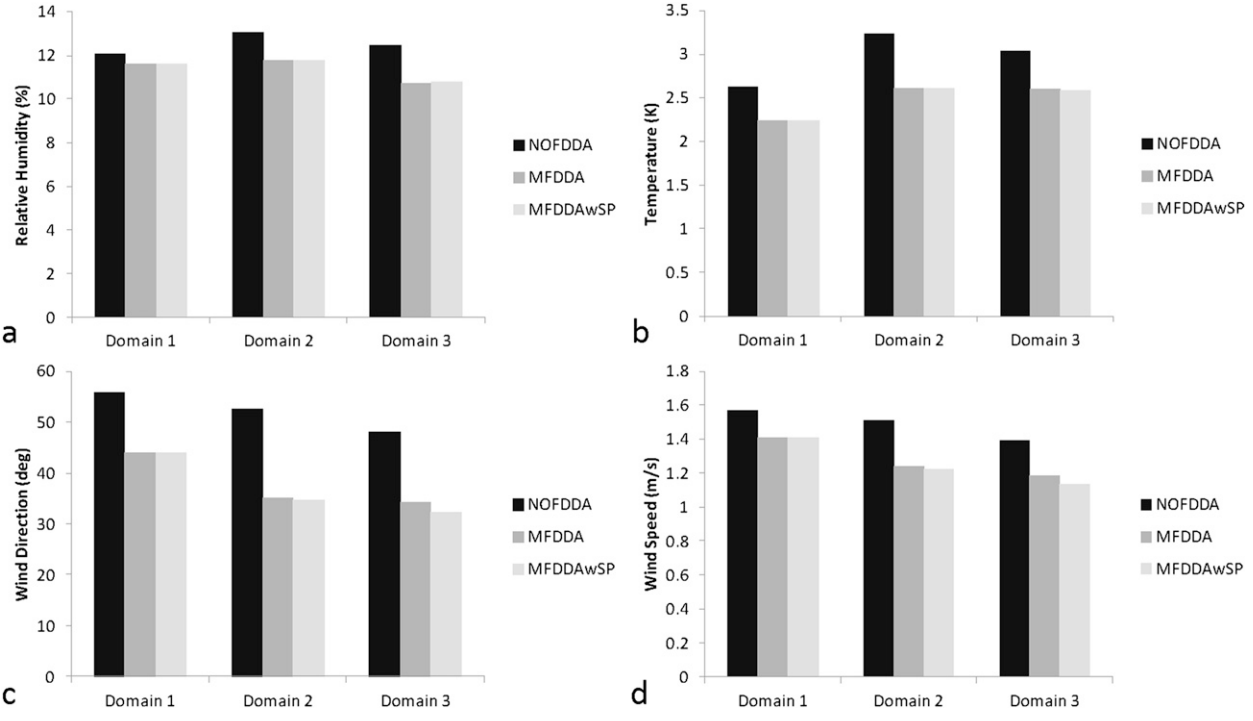

FIG. 9. Surface MAEs for the summer ozone case, averaged over the entire 5-day period and over the entire grid for each grid starting 1200 UTC 29 Jul and ending 1200 UTC 3 Aug 2000 comparing NOFDDA, MFDDA, and MFDDAwSP for the WRF-simulated fields: (a) RH, (b) temperature, (c) wind direction, and (d) wind speed.

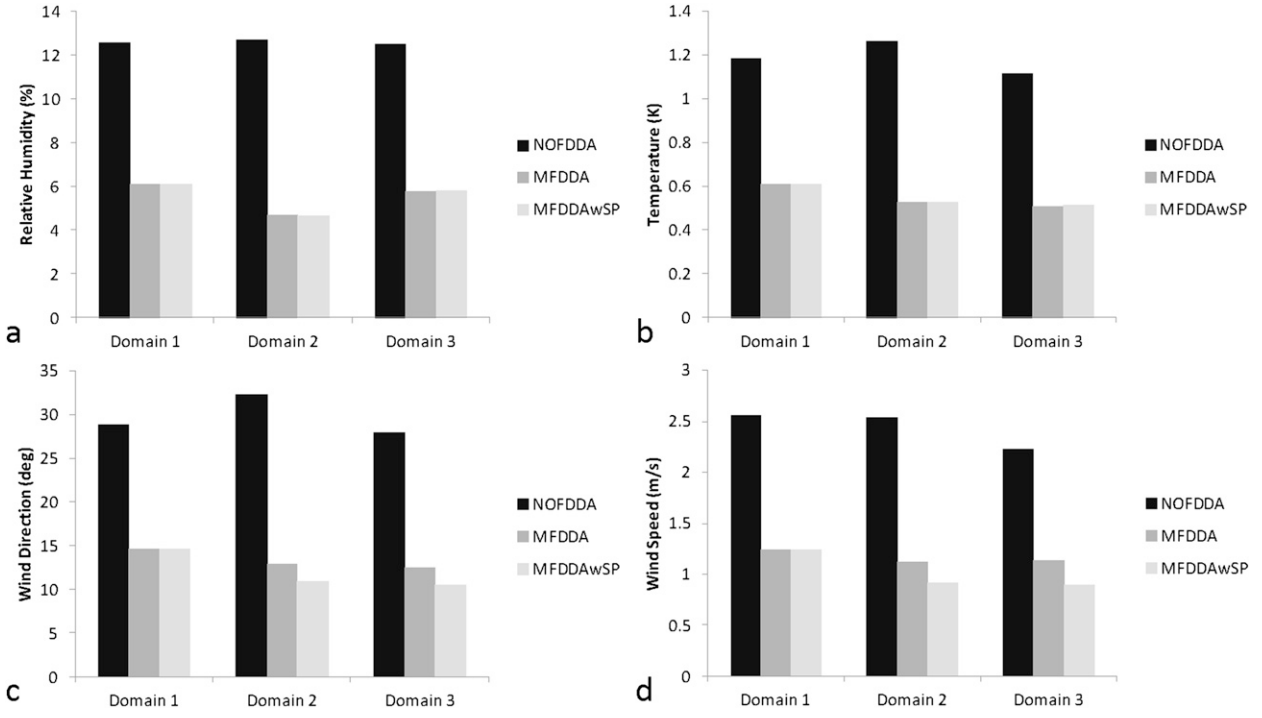

FIG. 10. As in Fig. 9, but for upper-air MAEs.

southern SJV. In MFDDAwSP (Fig. 5b), the overall wind patterns simulated by the model show better agreement with the observations than for NOFDDA. Examples include the winds along the coast and over the ocean, in the SV, and in the southern end of the SJV near Bakersfield.

The examination of particular observation sites can be of importance to understanding how the meteorology of a region can influence local stations. Three locations are chosen: Livermore, Sacramento, and Fresno, each representing a specific subregion mentioned above. Figure 6 shows the time series of the WRF-predicted first model layer (~10 m AGL) temperature and wind fields, comparing NOFDDA and MFDDAwSP with the observed values at Livermore. For temperature (Fig. 6a), both simulations do a good job of simulating the diurnal temperature cycle in the daytime, and tend to have a warm bias in the nighttime, which is reduced in MFDDAwSP. The warm bias corresponds to calm wind periods at this location (Fig. 6b), indicating that the PBL scheme may fail to simulate the temperature under nighttime stable conditions, or that the LSM inaccurately simulated the surface heat fluxes. For wind speed (Fig. 6b), both observations and model simulations show weak diurnal variations, but there is little effect from using FDDA. The fact that the wind speed observations show unrealistic oscillations at lower-speed ranges may indicate an instrument issue. For wind direction (Fig. 6c), consistent with the observations, both simulations show easterly flow, representing the northeasterly flow that converges with the northwesterly marine flow in the Livermore valley.

At Sacramento, both simulations developed the temperature diurnal cycles and agreed very well with the observations (Fig. 7a). The wind speeds were nearly calm for most of the period, except during the second day when the winds are very high (~12 m s^{-1}) when a front passed (Fig. 7b). The near-calm winds after the second day represent the time when the high-PM episode occurred in the CV. Both simulations agreed very well with the observations throughout the period except they had slower than observed wind speeds during the second day when the front passed, and FDDA has smaller biases. The wind direction time series (Fig. 7c) shows both simulations had the wind direction change between northwesterly and northeasterly repeatedly, except for the second day, where the winds were northerly when the front passed. Notice that the wind direction adjusting due to use of FDDA is somewhat evident (e.g., near 7, 72, and 84 h).

At Fresno, both simulations agreed well with the temperature observations (Fig. 8a). During the second day the front kept temperatures cool, and both simulations had cold biases for about the first 70 h. There is no evident benefit of using FDDA except for the first day. For wind speed, the observations show high-frequency oscillations throughout the period (Fig. 8b), indicating potential instrument issues that require further investigation. For wind direction, both simulations show clear

TABLE 7. WRF-simulated surface MAEs verified against the AQS independent dataset, for the summer ozone case, averaged over the entire 5-day period and over the entire grid for each grid, starting 1200 UTC 29 Jul and ending 1200 UTC 3 Aug 2000, comparing NOFDDA and MFDDAwSP. Note that RH was unavailable.

	36 km	12 km	4 km
Temperature			
NOFDDA	3.0	3.1	2.9
MFDDAwSP	2.8	2.8	2.7
Wind direction			
NOFDDA	55	48	51
MFDDAwSP	51	38	39
Wind speed			
NOFDDA	1.4	1.4	1.3
MFDDAwSP	1.3	1.2	1.2

diurnal signals with the wind directions (Fig. 8c), unlike the wind speed. Winds are easterly at night, representing the downslope flow off the Sierra Nevada, and westerly during the day, representing the flow up the mountains. With a limited number of observations, MFDDAwSP seems to have a better level of agreement with the observed wind directions.

b. *Summer ozone case*

1) QUANTITATIVE VERIFICATION

This case had synoptic conditions similar to those of the winter case where there was very little moisture and precipitation throughout the period. The same radiation suite, RRTM/Dudhia, used for the winter case is also used for this the summer ozone case, and similar to the winter case, three LSMs are evaluated.

Table 6 shows the WRF-simulated surface MAE, averaged over the entire 5-day period and over the entire grid for each grid, comparing the Noah, RUC, and the PX LSMs, for all four meteorological fields. Overall, no particular LSM is better than the other two. Since the PX scheme is developed by the U.S. Environmental Protection Agency and has been widely used for air quality applications and worked for the winter case, it is chosen as the land surface model for use in the FDDA simulations for this case, along with the RRTM/Dudhia radiation scheme.

Figure 9 shows the WRF-simulated surface MAEs for all experiments. Comparing Figs. 9a and 9b shows that using FDDA reduces the RH and temperature errors

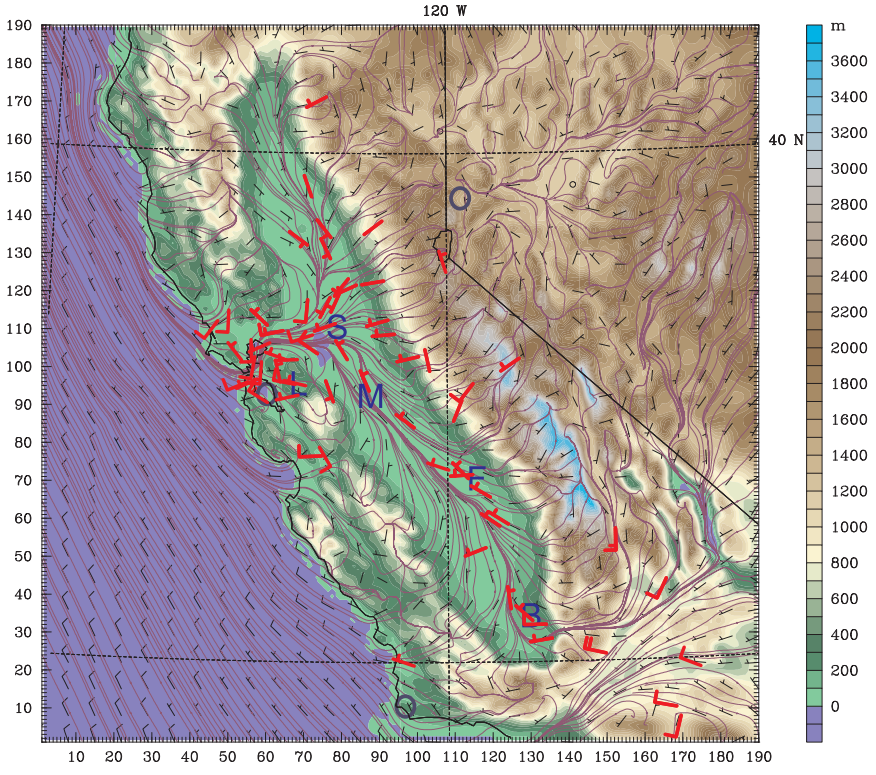

FIG. 11. WRF-simulated surface layer winds on the 4-km grid overlaid with observations at 0000 UTC 30 Jul 2000 from MFDDAwSP. Note that the large open circles denote the locations of the three WMO-upper air stations (Oakland, Reno, and Vandenberg Air Force Base), and other symbols mark the locations of Livermore (L), Fresno (F), Sacramento (S), Bakersfield (B), and Modesto (M). The background shading shows the terrain elevation (m).

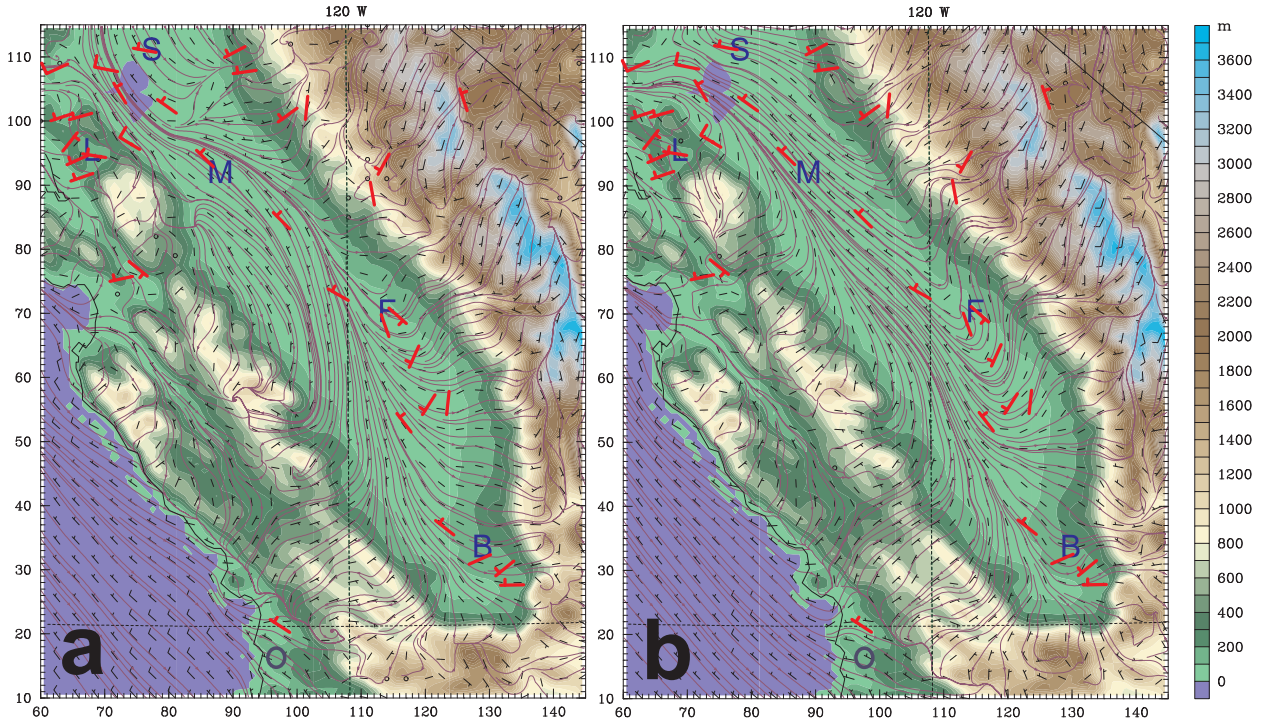

FIG. 12. WRF-simulated surface layer winds on the 4-km grid over a subregion covering the SJV overlaid with observations at 1800 UTC 30 Jul 2000 for (a) NOFDDA and (b) MFDDAwSP. Note that the large open circle denotes the location of the Vandenberg Air Force Base WMO upper-air station, and other symbols mark the locations of Livermore (L), Fresno (F), Sacramento (S), Bakersfield (B), and Modesto (M). The background shading shows the terrain elevation (m).

even though no FDDA is applied for mass fields within the PBL. The largest relative improvement is in the wind direction field (Fig. 9c), and only a slight improvement is seen in the wind speed (Fig. 9d). The ME (not shown) indicates that the model tends to be slightly more moist ($\sim+5\%$) and cooler (~-0.6 to -1.2°C) than the observations. There is a very small bias for the wind direction (<3°) and the speed is slightly slower ($<0.6\,\mathrm{m\,s^{-1}}$). FDDA does not seem to reduce the bias.

Figure 10 shows that FDDA in the upper air has allowed both MFDDA simulations to reduce the RH errors (e.g., by ~8% on the 4-km grid) and the temperature errors (e.g., by 0.6°C on the 4-km grid) relative to the NOFDDA simulation (Figs. 10a and 10b). The MFDDA simulations also reduced the wind direction errors (e.g., by 18° on the 4-km grid in MFDDAwSP) and the wind speed errors (e.g., by $1.5\,\mathrm{m\,s^{-1}}$ on the 4-km grid in MFDDAwSP) relative to NOFDDA (Figs. 10c and 10d). The ME scores (not shown) indicate that the upper-air biases for all four meteorological fields are much smaller than the surface biases. The model has slight biases in temperature, wind direction, and wind speed. Overall, both FDDA experiments have smaller biases than the NOFDDA experiment.

Similar to the winter case, the added value of assimilating the special AQS surface observations can be shown by comparing the MAEs of the model-simulated fields between MFDDA and MFDDAwSP. For both surface (Fig. 9) and upper-air (Fig. 10) cases, the benefit of using the AQS data, though small, is evident in the wind fields, especially on the finer grids.

Similar to the winter case, both NOFDDA and MFDDAwSP are compared with the independent set of 72 observations that are not assimilated. Table 7 shows the WRF-simulated surface MAEs, averaged over the entire 5-day period and over the entire grid for each grid. MFDDAwSP performs better than NOFDDA for all the fields, showing slight improvement in the temperature errors and the wind speed errors but showing somewhat larger improvement in the wind direction errors. This independent verification demonstrates again that multiscale FDDA is an effective technique for reducing model errors and producing high-quality gridded mesoscale analyses for use in air quality applications.

The statistics analysis for the subregions (not shown) indicates that in the SFBA region both NOFDDA and MFDDAwSP produce nearly the same errors for the surface RH and temperature, with some slight degradations for MFDDAwSP. FDDA does improve the surface wind direction and the wind speed due to the assimilation of the surface wind observations. For the upper air, FDDA reduces the errors on all four fields. Comparing

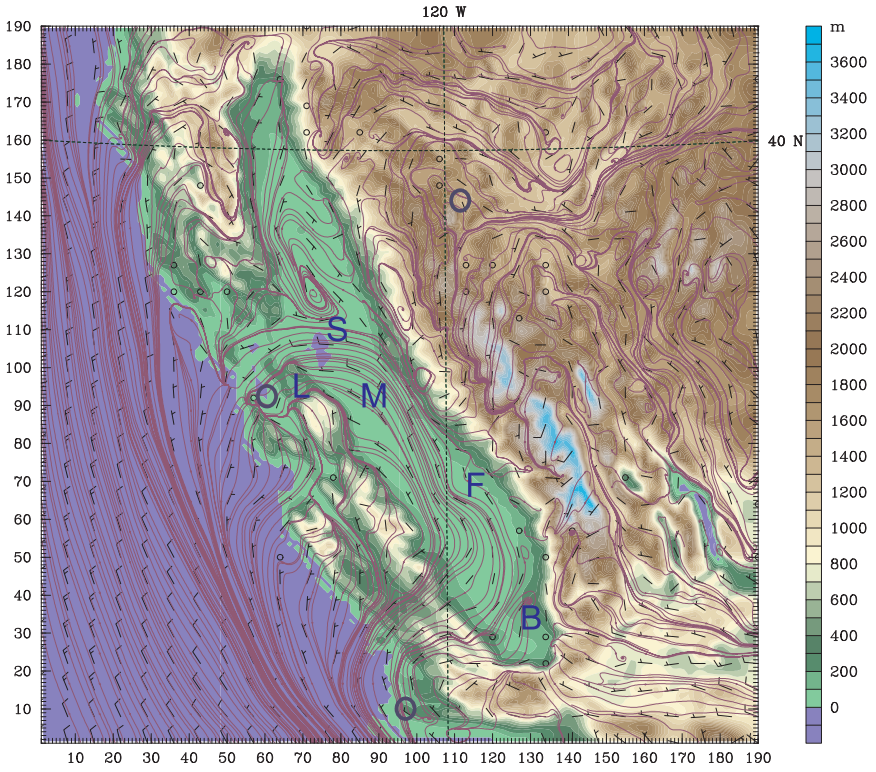

FIG. 13. WRF-simulated winds on the 4-km grid at the ninth model level (i.e., ~300 m above the ground) at 1200 UTC 30 July 2000 for MFDDAwSP. Note that the large open circles denote the locations of the three WMO upper-air stations (Oakland, Reno, and Vandenberg Air Force Base), and other symbols mark the locations of Livermore (L), Fresno (F), Sacramento (S), Bakersfield (B), and Modesto (M). The background shading shows the terrain elevation (m).

the SFBA statistics with that of the entire 4-km grid, it is again found that the FDDA is not as effective over the SFBA region. The MAEs for both the SV and SJV are similar to those for the entire 4-km grids. MFDDAwSP slightly improves RH, *T*, and wind speed while significantly improving wind direction, unlike in the SFBA region. Note that there are no upper-air statistics available for both regions because the only upper-air stations within the 4-km grid are outside both subregions.

2) QUALITATIVE VERIFICATION

On the 36-km grid, both NOFDDA and MFDDAwSP do a good job of simulating the surface synoptic conditions throughout the period, similar to the winter case. Both are in good agreement with the placement of highs and lows, the temperature pattern, and the onshore and offshore flows along the coast. However, at 850 hPa, MFDDAwSP represents the pressure gradients around the observed high off the coast of California better than NOFDDA does (not shown) and also better represents the winds over the coast. At 500 hPa, both simulations do a reasonable job of representing the observed patterns.

To demonstrate the model's skill in representing the typical daytime flow pattern, Fig. 11 shows the WRF-simulated surface-layer winds on the entire 4-km grid at 0000 UTC 30 July 2000, 12 h into the simulation for MFDDAwSP, representing the local afternoon conditions. The simulated winds from both simulations (NOFDDA not shown) follow the conceptual model from Bao et al. (2008) for the daytime. The westerly winds coming onshore over the SFBA represent the incoming marine flow that passes through the Carquinez Strait and into the CV, where it splits into two main branches (represented by the densely packed streamlines): 1) southerly flow up the SV and 2) northerly flow with a low-level jet down the SJV. The heating of the mountaintops all along the CV creates upslope flows. At the southern end of the SJV the northerly mean flow leaves the valley through the Tehachapi Mountains.

The effect of FDDA is demonstrated over the SJV in Fig. 12 by the WRF-simulated surface-layer winds, at 1800 UTC 30 July 2000, when the daytime pattern has developed in both simulations. The overall flow patterns in both simulations are generally similar, but smaller-scale details (e.g., upslope winds over Fresno area) are

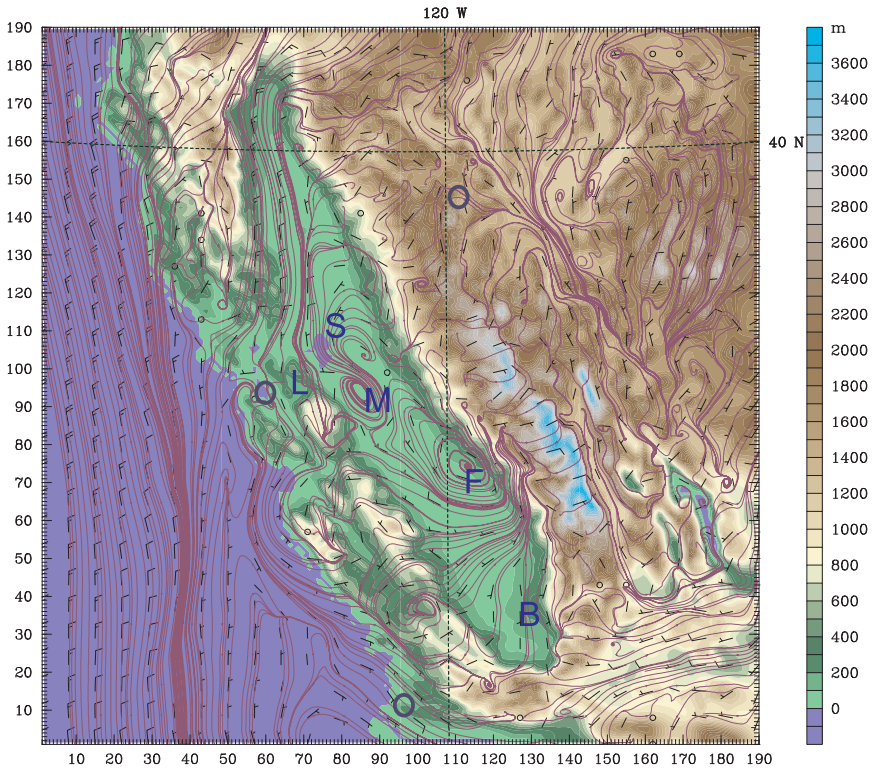

FIG. 14. As in Fig. 13, but for WRF-simulated surface layer winds on the 4-km grid at the ninth model level (i.e., ~300 m above the ground) at 1200 UTC 1 Aug 2000 for MFDDAwSP.

better defined in the MFDDAwSP. It is important to show the model's skill in simulating the low-level mesoscale features (e.g., the Schultz eddy and Fresno eddy) that has been well documented in previous modeling studies (e.g., Seaman et al. 1995; Lin and Jao 1995; Bao et al. 2008).

Figure 13 shows the WRF-simulated winds at 1200 UTC 30 July 2000, 24 h into the simulation, at about 300 m above the ground (i.e., the ninth model level from the surface). MFDDAwSP represents the incoming marine flow over the SFBA better than NOFDDA (not shown). Both develop the downslope flow from the mountaintops along the CV. This downslope flow then converges with the main bulk northerly flow down both the SV and the SJV. The downslope flow from the Sierra Nevada northeast of Sacramento is southeasterly before crossing the valley and turning northerly to converge with the mean flow; this southerly flow and the northerly bulk flow develop the Schultz eddy. The Schultz eddy is located just northwest of Sacramento and appear farther south in MFDDAwSP than in the NOFDDA, and thus agrees better with the nighttime conceptual model from Bao et al. (2008).

The existence of the Fresno eddy is demonstrated in Fig. 14, which shows the simulated low-level winds (at the same ninth model level from the surface) from MFDDAwSP at 1200 UTC 1 August 2000. Both simulations develop the Fresno eddy at this time. However, NOFDDA also develops a second eddy over Bakersfield, near the southern end of SJV (not shown), while MFDDAwSP develops a second eddy near Modesto, close to the northern end of the SJV.

Similar to the winter PM case, the same three locations are chosen to demonstrate the model skills at each of the specific subregions. At Livermore in the SFBA, the model well simulates the diurnal temperature cycles throughout the 5-day period while there is a slight cold bias in both simulations during the daytime (Fig. 15a). At nighttime, NOFDDA tends to have warm biases that are corrected by FDDA. In addition, the observations and the model both show a slight warming trend throughout the 5-day simulation. The model also does a good job of simulating a diurnal pattern in the wind speeds where the fastest winds occur during the day, although the simulated wind speeds in both simulations are systematically too slow during the daytime (Fig. 15b). MFDDAwSP is in better phase with the observations than NOFDDA in the morning. However, for wind direction (Fig. 15c), the benefit of FDDA is not evident and there are no clear diurnal cycles. In contrast, the nearby station of

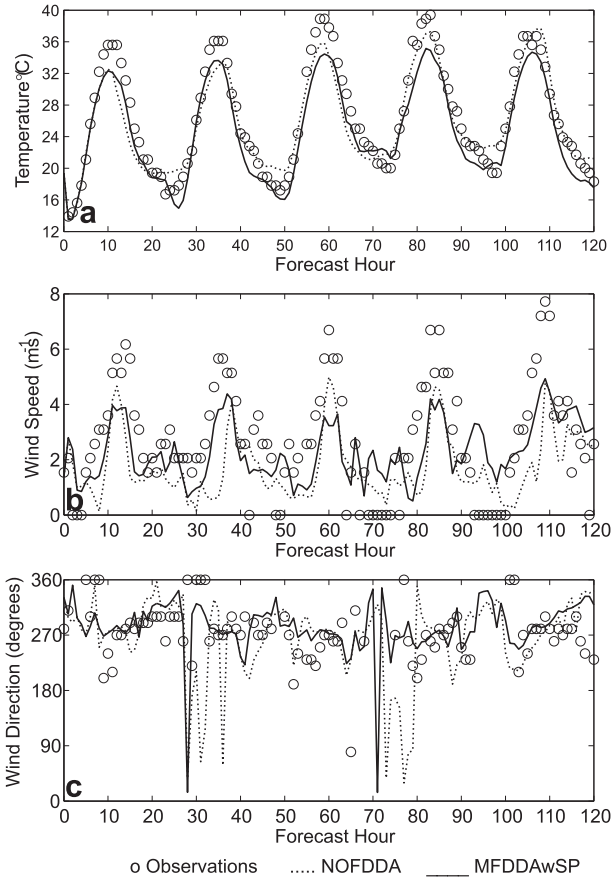

FIG. 15. WRF-simulated fields and the observed surface time series plot for Livermore, for the summer ozone case, starting 1200 UTC 29 Jul and ending 1200 UTC 3 Aug 2000, for (a) temperature, (b) wind speed, and (c) wind direction.

Pleasanton shows clear diurnal cycles between the brief easterly flow in the morning and the persistent westerly flow during the rest of the day (not shown). It is possible that the difference between these two nearby stations is caused by the fact that Pleasanton is closer to the mountains to the west, while Livermore is located in the middle of the valley so that the terrain effect is dominant for Pleasanton. This terrain effect only lasts a few hours before the bulk westerly flow takes over. The limited representativeness of the observations likely causes FDDA not to perform as well as it does for the whole grid.

In the SV, both simulations do a good job of simulating the diurnal temperature cycles and the warming trend (Fig. 16a). During the first 3 days the model is slightly cooler than the observations during the day, and the benefit of FDDA appears evident only on the second day. For wind speed (Fig. 16b), the observed diurnal variations are well reproduced by both simulations. Notice that the observations show that large wind speed oscillations occur during nearly every hour and MFDDAwSP also follows these quick changes. Since these oscillations also exist in NOFDDA, it is possible these are the signals of the transient motions (e.g., gravity waves) passing though the site. Similar oscillations are also seen in the observed and modeled wind directions, and there is some apparent benefit to using FDDA (Fig. 16c).

In the SJV (Fig. 17), at Fresno, both simulations tend to be cooler than the observations by several degrees, and no clear advantage is found with the use of FDDA (Fig. 17a). This is probably due to the land surface model not properly representing the characteristics of the valley region. It is also possible that the deep soil temperature in the PX LSM was not adequately spun up, which can be made possible in the BAAQMD's operational model runs in the future. For wind speed (Fig. 17b), similar to the winter PM case, the observations show high-frequency oscillations, but the model does not simulate all the quick changes, unlike at Sacramento. Similar to the observations, the model shows weak diurnal cycles but tends to have lower speeds than the observations, likely a response to cooler daytime temperatures and less mixing from free atmospheric flow aloft. The model develops a diurnal pattern for the wind direction, with northeasterly winds during the night representing the downslope flow from the Sierra Nevada and westerly winds during the day representing the flow up the mountains (Fig. 17c). Overall, MFDDAwSP is in better agreement with the observations than NOFDDA.

c. *Discussion on optimal radius of influence*

The obs-nudging technique uses a radius of influence to determine which individual observations have an influence on the model solution at each grid point. The RIN is theoretically represented by the horizontal distance within which the model errors at different locations are correlated, and is normally chosen based on previous modeling studies (Stauffer and Seaman 1994; Deng et al. 2009). To verify that the RIN used in this study is within a reasonable range, error correlations were computed from 10 observation sites selected at various locations within the 4-km grid. The temperature innovations (i.e., the difference between the observation and the model value) from the NOFDDA simulations at those sites were used to calculate the correlation between pairs of sites for all the sites. Figure 18 shows the correlation coefficients versus the horizontal distance between various pairs of observation sites. Thirteen coefficients are shown to provide a good distribution of the horizontal distances and to provide a good distribution for high and low coefficients. For this experiment the largest correlation is at 63 km, which indicates that the selected RIN value (i.e., 50 km at the surface) used in this research is reasonable.

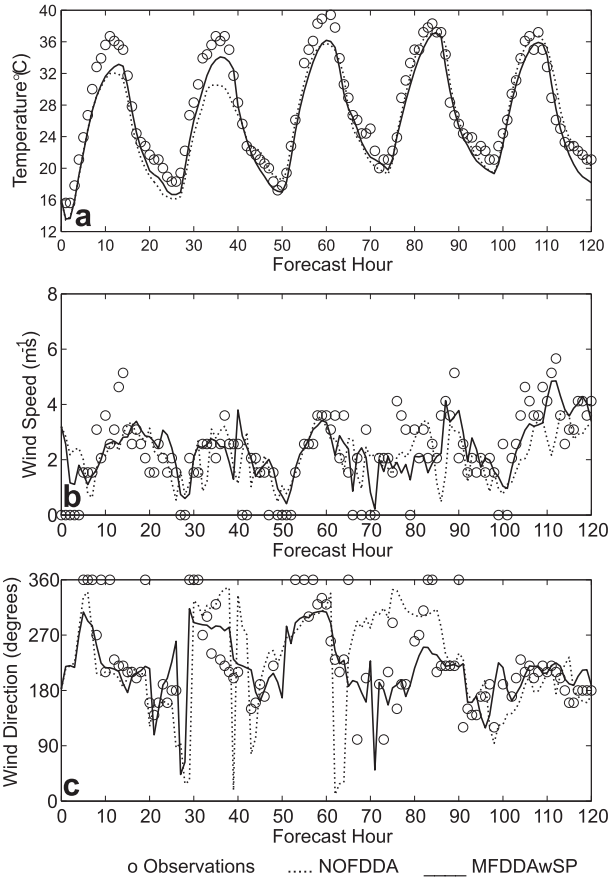

FIG. 16. As in Fig. 15, but for Sacramento.

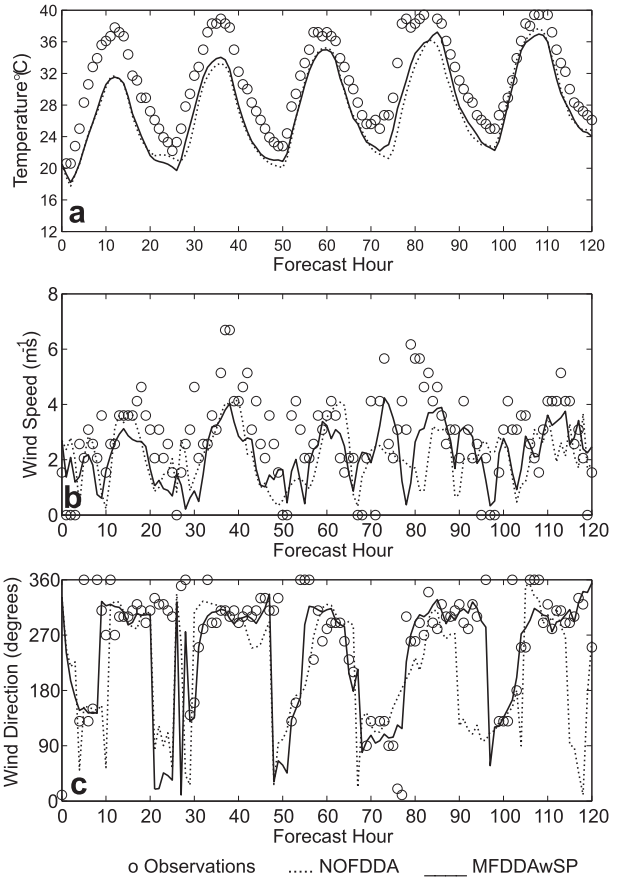

FIG. 17. As in Fig. 15, but for Fresno.

6. Conclusions

The goal of this research was to establish a recommended configuration for the WRF modeling system to be used at BAAQMD for its operational air quality modeling applications that use the CMAQ model to simulate the air-pollutant distributions over the SFBA region. Various WRF sensitivity simulations were conducted with varying model physics and FDDA strategies. It was found based on both quantitative and qualitative verifications that, for both the winter and summer cases, WRF performs quite well in producing simulations that have reasonable error statistics and in capturing the realistic mesoscale features in the valleys.

The investigation began with setting up a baseline configuration before FDDA was applied throughout the simulations. This was achieved by testing and evaluation of different radiation schemes and land surface models. It was found that both radiation suites and the four LSMs performed similarly, with the exception that PX LSM had a clear advantage for the winter PM case. Therefore, for both the winter and summer cases, the RRTM/Dudhia radiation suite and the PX LSM were chosen for the baseline configuration, with which a number of FDDA strategies were explored: 1) analysis nudging, 2) obs nudging, and 3) a multiscale FDDA that combined both analysis nudging and obs nudging. For the winter PM, using FDDA reduced the model errors, with the multiscale FDDA strategy producing the smallest errors for all four fields. Similarly, for the summer ozone case, the multiscale FDDA strategy significantly reduced the mode errors. The FDDA simulations performed better than the NOFDDA simulations when they were compared over subregions within the 4-km grid but the improvements were somewhat smaller for the SFBA region due to the complexity of the local topographical features and the limited representativeness of the observations. The FDDA simulations also performed better than the NOFDDA simulation when they were compared against an independent dataset. For both winter and summer cases, there was an advantage to using the AQS observations in further improving the model solutions, particularly in wind fields.

Qualitative analysis showed that even without FDDA, WRF can represent the humidity, temperature, and wind fields reasonably well for both cases. On the large scale

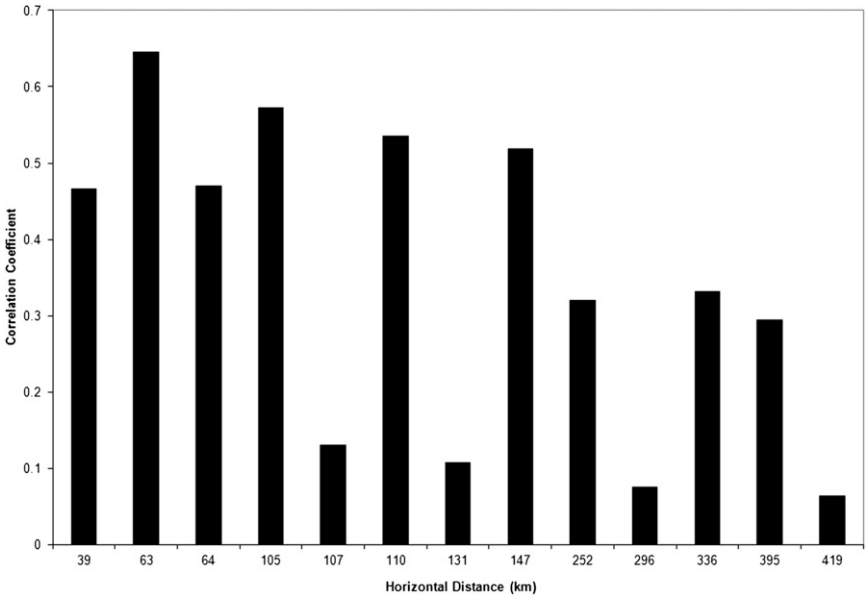

FIG. 18. Model error correlation coefficient vs horizontal distance between various pairs of surface observation sites.

the locations of WRF-simulated high and low pressure regions on the 36-km grid were well placed and the large-scale wind patterns were consistent with the observations. Using the multiscale FDDA strategy improved the wind patterns the most, and troughs and ridges were simulated with a good degree of accuracy. On the 4-km grid even without FDDA, WRF was shown to simulate the mesoscale wind patterns reasonably well for both cases. The simulations with and without FDDA can develop the upslope and downslope flows that occur along the mountains that surround the CV, as well as the mesoscale eddies within the valley. The multiscale FDDA simulations develop the mesoscale eddies in better agreement with the observations than do the non-FDDA experiments.

To help evaluate the WRF performance in each subregion, times series at a selected site within each subregion were analyzed. It was found that in the SFBA, WRF showed a nighttime warm bias along with a slight cold bias during the daytime for the winter PM case, and a slight warm bias at nighttime for the summer ozone case. FDDA, in general, corrects these surface temperature biases despite temperature data not being assimilated into the PBL. For the surface winds, the effect of FDDA was not evident, except that for the summer ozone case, FDDA tried to correct the phase error in the wind speed during morning times. In Sacramento, WRF, with and without FDDA, developed the temperature diurnal cycle and agreed very well with the observations for both winter PM and for summer ozone cases. For wind fields, both simulations (for both cases) agreed quite well with the observations throughout the period, and FDDA had a somewhat positive effect in causing the model to track the observations. For the summer ozone case, there were transient waves shown in both the model and observations. In the SJV, for both the winter PM and summer ozone cases, WRF showed systematic cold biases at Fresno. The use of FDDA did not completely resolve this issue. For surface winds, the WRF was able to reproduce the observed up- and downslope motions, as well as the diurnal variations. The multiscale FDDA simulations agree better with the observations than does the non-FDDA simulation.

Ten observation sites were chosen at various locations within the 4-km grid, and the temperature innovation values from the non-FDDA model simulation at those sites were used to calculate the error correlation between two sites. Results showed that the 50-km RIN value used in the obs nudging of the surface observations was reasonable.

Future research will include simulations with improved model resolution, especially over the SFBA, and improved FDDA strategies such as the new, advanced, hybrid nudging–ensemble Kalman filter method developed at Penn State (Lei et al. 2012). This hybrid approach automatically and objectively determines the nudging weights, and the effective horizontal and vertical radii of influence based on the ensemble error covariance statistics and, thus, removes the requirement for defining ad hoc nudging weights and radii of influence. Future

work will also include better deep soil temperature initialization by running the model for at least 10 days.

Acknowledgments. This research was funded by the Bay Area Air Quality Management District, under Contract 2009-078. We thank Dr. Brian Reen for providing guidance on the use of WRF obs nudging functionalities. We also thank Dr. George Young and Glenn Hunter for helping with model evaluation and Astrid Suarez for assisting with the figures.

REFERENCES

Bao, J.-W., S. A. Michelson, P. O. G. Persson, I. V. Djalalova, and J. M. Wilczak, 2008: Observed and WRF-simulated low-level winds in a high-ozone episode during the Central California Ozone Study. *J. Appl. Meteor. Climatol.,* **47,** 2372–2394.

Benjamin, S. O., and N. L. Seaman, 1985: A simple scheme for objective analysis in curved flow. *Mon. Wea. Rev.,* **113,** 1184–1198.

Byun, D., and K. L. Schere, 2006: Review of the governing equations, computational algorithms, and other components of the Models-3 Community Multiscale Air Quality (CMAQ) modeling system. *Appl. Mech. Rev.,* **59,** 51–77.

Chen, F., and J. Dudhia, 2001: Coupling an advanced land surface–hydrology model with the Penn State–NCAR MM5 modeling system. Part I: Model implementation and sensitivity. *Mon. Wea. Rev.,* **129,** 569–585.

Deng, A., N. L. Seaman, G. K. Hunter, and D. R. Stauffer, 2004: Evaluation of interregional transport using the MM5–SCIPUFF system. *J. Appl. Meteor.,* **43,** 1864–1886.

——, and Coauthors, 2009: Update on WRF-ARW end-to-end multi-scale FDDA system. *10th Annual WRF Users' Workshop,* Boulder, CO, NCAR, 1.9. [Available online at http://www.mmm.ucar.edu/wrf/users/workshops/WS2009/abstracts/1-09.pdf.]

Dudhia, J., 1989: Numerical study of convection observed during the Winter Monsoon Experiment using a mesoscale two-dimensional model. *J. Atmos. Sci.,* **46,** 3077–3107.

Gilliam, R. C., and J. E. Pleim, 2010: Performance assessment of new land surface and planetary boundary layer physics in the WRF-ARW. *J. Appl. Meteor. Climatol.,* **49,** 760–774.

——, C. Hogrefe, and S. T. Rao, 2006: New methods for evaluating meteorological models used in air quality applications. *Atmos. Environ.,* **40,** 5073–5086.

Grell, G. A., J. Dudhia, and D. R. Stauffer, 1994: A description of the fifth-generation Penn State/NCAR Mesoscale Model (MM5). NCAR Tech. Note NCAR/TN-398+STR, 128 pp.

Hong, S.-Y., J. Dudhia, and S.-H. Chen, 2004: A revised approach to ice microphysical processes for the bulk parameterization of clouds and precipitation. *Mon. Wea. Rev.,* **132,** 103–120.

Iacono, M., J. Delamere, E. Mlawer, M. Shephard, S. Clough, and W. Collins, 2008: Radiative forcing by long-lived greenhouse gases: Calculations with the AER radiative transfer models. *J. Geophys. Res.,* **113,** D13103, doi:10.1029/2008JD009944.

Janjić, Z. I., 1996: The surface layer in the NCEP Eta Model. Preprints, *11th Conf. on Numerical Weather Prediction,* Norfolk, VA, Amer. Meteor. Soc., 354–355.

——, 2002: Nonsingular implementation of the Mellor–Yamada level 2.5 scheme in the NCEP Meso Model. NCEP Office Note 437, 107 pp.

Kain, J. S., 2004: The Kain–Fritsch convective parameterization: An update. *J. Appl. Meteor.,* **43,** 170–181.

——, and M. Fritsch, 1990: A one-dimensional entraining/detraining plume model and its application in convective parameterization. *J. Atmos. Sci.,* **47,** 2784–2802.

Kumar, N., and F. W. Lurmann, 1997: Peer review of ENVIRON's ozone source apportionment technology and the CAMx air quality model. Revised Final Rep. STI-996203-1732-RFR, Division of Air Pollution Control, Ohio Environmental Protection Agency, Columbus, OH, 34 pp.

Lei, L., D. R. Stauffer, and A. Deng, 2012: A hybrid nudging–ensemble Kalman filter approach to data assimilation in WRF/DART. *Quart. J. Roy. Meteor. Soc.,* **138B,** 2066–2078, doi:10.1002/qj.1939.

Leidner, S. M., D. R. Stauffer, and N. L. Seaman, 2001: Improving short-term numerical weather prediction in the California coastal zone by dynamic initialization of the marine boundary layer. *Mon. Wea. Rev.,* **129,** 275–294.

Lin, Y.-L., and I.-C. Jao, 1995: A numerical study of flow circulations in the Central Valley of California and formation mechanisms of the Fresno eddy. *Mon. Wea. Rev.,* **123,** 3227–3239.

Michelson, S. A., and J.-W. Bao, 2008: Sensitivity of low-level winds simulated by the WRF model in California's Central Valley to uncertainties in the large-scale forcing and soil initialization. *J. Appl. Meteor. Climatol.,* **47,** 3131–3149.

Mlawer, E. J., S. J. Taubman, P. D. Brown, M. J. Iacono, and S. A. Clough, 1997: Radiative transfer for inhomogeneous atmosphere: RRTM, a validated correlated-k model for the longwave. *J. Geophys. Res.,* **102** (D14), 16 663–16 682.

Oreopoulos, L., and Coauthors, 2012: The Continual Intercomparison of Radiation Codes: Results from phase I. *J. Geophys. Res.,* **117,** D06118, doi:10.1029/2011JD016821.

Otte, T. L., 2008a: The impact of nudging in the meteorological model for retrospective air quality simulations. Part I: Evaluation against national observation networks. *J. Appl. Meteor. Climatol.,* **47,** 1853–1867.

——, 2008b: The impact of nudging in the meteorological model for retrospective air quality simulations. Part II: Evaluating collocated meteorological and air quality observations. *J. Appl. Meteor. Climatol.,* **47,** 1868–1887.

Pleim, J. E., 2007: A combined local and nonlocal closure model for the atmospheric boundary layer. Part I: Model description and testing. *J. Appl. Meteor. Climatol.,* **46,** 1383–1395.

——, and A. Xiu, 2003: Development of a land surface model. Part II: Data assimilation. *J. Appl. Meteor.,* **42,** 1811–1822.

——, and R. Gilliam, 2009: An indirect data assimilation scheme for deep soil temperature in the Pleim–Xiu land surface model. *J. Appl. Meteor. Climatol.,* **48,** 1362–1376.

Schroeder, A., D. R. Stauffer, N. L. Seaman, A. Deng, A. Gibbs, G. K. Hunter, and G. S. Young, 2006: An automated high-resolution, rapidly relocatable meteorological nowcasting and prediction system. *Mon. Wea. Rev.,* **134,** 1237–1265.

Seaman, N. L., D. R. Stauffer, and A. M. Lario-Gibbs, 1995: A multiscale four-dimensional data assimilation system applied in the San Joaquin Valley during SARMAP. Part I: Modeling design and basic performance characteristics. *J. Appl. Meteor.,* **34,** 1739–1761.

Skamarock, W. C., and Coauthors, 2008: A description of the Advanced Research WRF version 3. NCAR Tech. Note NCAR/TN-475+STR, 113 pp.

Smirnova, T. G., J. M. Brown, and S. G. Benjamin, 1997: Performance of different soil model configurations in simulating

ground surface temperature and surface fluxes. *Mon. Wea. Rev.,* **125,** 1870–1884.

——, ——, ——, and D. Kim, 2000: Parameterization of cold season processes in the MAPS land-surface scheme. *J. Geophys. Res.,* **105** (D3), 4077–4086.

Soong, S.-T., and Coauthors, 2006: Comparison of WRF/CAMx and MM5/CAMx simulations for an ozone episode in California. Preprints, *Eighth Conf. on Atmospheric Chemistry/ 14th Joint Conf. on the Applications of Air Pollution Meteorology with the Air and Waste Management Association,* Atlanta, GA, Amer. Meteor. Soc., J1.4. [Available online at https://ams.confex.com/ams/pdfpapers/104587.pdf.]

Stauffer, D. R., and N. L. Seaman, 1990: Use of four-dimensional data assimilation in a limited-area mesoscale model. Part I: Experiments with synoptic-scale data. *Mon. Wea. Rev.,* **118,** 1250–1277.

——, and ——, 1994: Multiscale four-dimensional data assimilation. *J. Appl. Meteor.,* **33,** 416–434.

Tanrikulu, S., D. R. Stauffer, N. L. Seaman, and A. J. Ranzieri, 2000: A field-coherence technique for meteorological field-program design for air quality studies. Part II: Evaluation in the San Joaquin Valley. *J. Appl. Meteor.,* **39,** 317–334.

Watson, J. G., and Coauthors, 1998: Aerometric monitoring program plan for the California regional PM2.5/PM10 air quality study. DRI Document 9801.1D5, 354 pp.

Xiu, A., and J. E. Pleim, 2001: Development of a land surface model. Part I: Application in a mesoscale meteorological model. *J. Appl. Meteor.,* **40,** 192–209.